Ethene oligomerization on nickel microporous and mesoporous-supported catalysts: Investigation of the active sites

Ethene oligomerization on nickel microporous and mesoporous-supported catalysts: investigation of the active sites

Reynald Henry[1], Mustafa Komurcu[1], Yadolah Ganjkhanlou[3], Rasmus Y. Brogaard[1], Li Lu[2], Klaus-Joachim Jens[2], Gloria Berlier[3*], Unni Olsbye[1**]

[1] Department of Chemistry, University of Oslo, P.O. Box 1033, Oslo 0315, Norway

[2] Faculty of Technology, University College of Southeast Norway, P.O.Box 203, Porsgrunn 3901, Norway

[3] University of Turin, Department of Chemistry IFM and NIS-Centre of Excellence, Via P. Giuria 7, Turin 10125, Italy

* gloria.berlier@unito.it

** unni.olsbye@kjemi.uio.no

Abstract

Nickel-containing mesoporous (using Al_2O_3 or SiO_2-Al_2O_3 support) and microporous (using nano- or micro-crystalline Beta zeolite support) catalysts were prepared by ion exchange and characterized by XRD, SEM, N_2-adsorption, MP-AES and FTIR. The samples were subjected to testing as ethene oligomerization catalysts at T = 120°C, P_{total} = 29 bar, P_{ethene} = 11.6–25.1 bar. All catalysts were active for ethene oligomerization, and linear butenes were the main gaseous products. However, catalyst deactivation due to retained long-chain alkenes was observed. Ethene partial pressure variation experiments showed that the reaction order in ethene for butene formation was 1.5-1.7 for the mesoporous, and 2.0 for the microporous catalysts. Contact time variation experiments carried out with the microporous catalysts at P(Ethene) = 18 bar showed that product selectivity was independent of ethene conversion, and suggested that 1-butene and 2-butenes are primary products. This result is consistent with the Cossee-Arlman mechanism. The nature of the active sites was investigated with FTIR spectroscopy with CO as probe molecule. The results points to Ni^{2+}-counterions as the preeminent active sites, while we suggest that Ni-sites grafted on silanol groups and NiO particles are spectators.

Introduction

The world is currently seeing a gradual shift from oil as the dominating source for transportation fuels and chemicals production to other alternative sources, such as natural gas, biomass and coal [1]. Traditionally, naphtha reforming has been the major source of low carbon olefins (C_2-C_6 alkenes), but the recent shift towards ethane cracking favors ethene production over the C_3-C_6 fraction. In addition the demand for propene and butenes has increased more rapidly than the demand for ethene [2]. This led to a growing interest in selective oligomerization of ethene to C_4-C_8 products [3, 4]. Ethene is among the most important base chemicals and has a worldwide production capacity over 130 million tons[2]. It is raw material for a wide range of products; reactions of ethene include oxidation, oligomerization and polymerization [4]. The commercial processes for ethene oligomerization utilizes homogeneous catalysts (transition metal catalysts in organic solvents [5]). In these processes, a co-catalyst such as $Al(C_2H_5)_3$ is required to start the catalytic cycle. The mechanism of alkene oligomerization with homogeneous catalysts has been reviewed by McGuinness [5] and the two widely recognized mechanisms, metallacycle and Cossee-Arlman, are shown in Scheme 1.

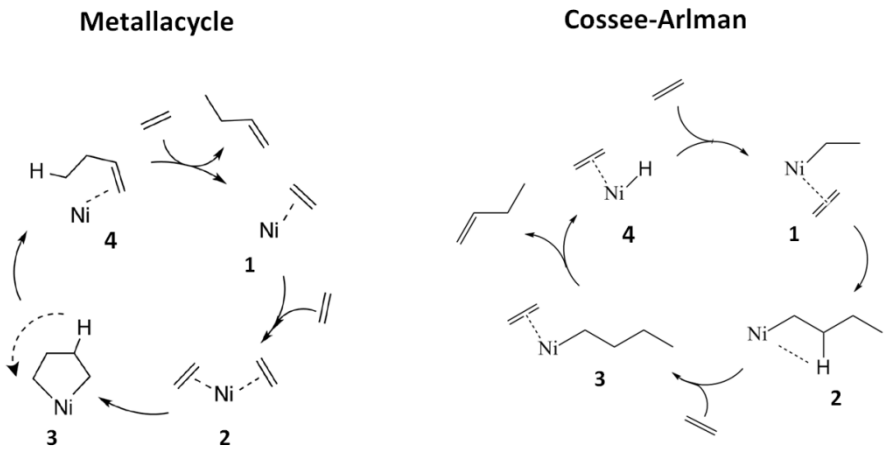

Scheme 1: The two widely recognized reaction mechanism for the homogeneously catalyzed oligomerization of ethene

In recent years, significant effort have been made to develop heterogeneous catalysts for the ethene oligomerization reaction, as they potentially offer a more environmentally friendly alternative to the homogeneously catalyzed process [4].

Nickel containing inorganic porous materials such as amorphous silica-alumina [6, 7], ordered mesostructured materials [8-10] and Ni-zeolites [11-13] are regarded as the most promising candidates among the reported catalysts. Notably, all these catalysts are active without the use of a

co-catalyst. The mesoporous catalysts are reported to perform better than microporous catalysts, which typically suffer from rapid deactivation due to blocking of micropores by alkenes formed during the reaction [12]. An exception is the nanocrystalline Ni-H-Beta zeolite, investigated at 120 °C and P_{ethene} = 26 bar, which was resistant to deactivation. The Ni-H-Beta catalysts were prepared by ion exchange of protons with Ni^{2+}. For these catalysts, the activity was reported to increase linearly with increasing Ni loading until almost all of the acid sites were exchanged. Furthermore, for catalysts with Ni content $\leq$ 2 % (i.e. with significant amounts of Brønsted acid sites remaining), approximately 93 % selectivity towards even numbered alkenes with Schulz-Flory type distribution were observed, suggesting that the acid sites have negligible activity for oligomerization under these conditions. However, the observed branching among the even numbered products was ascribed to the acid sites [13].

A detailed kinetic study of the ethene oligomerization reaction was recently published by Toch et al. [14] who investigated Ni-SiO_2-Al_2O_3 catalyst between 170 – 230 °C and P_{ethene} from 1.5 to 3.5 bar. They observed that the catalyst was resistant to deactivation during 8 h on stream and due to the absence of strong acid sites, they concluded the catalytic activity to be solely from the nickel ion sites. The catalyst showed Schulz-Flory type product distribution with about 90 % selectivity towards butenes while thermodynamic distribution was observed among the linear butenes. By combining experimentally obtained data with single event microkinetic modelling, they concluded the Cossee-Arlman mechanism to be more likely than the metallacycle mechanism because of the Schulz-Flory product distribution, without excluding the metallacycle mechanism completely [14].

Recently, Brogaard and Olsbye utilized molecular modelling to investigate the reaction mechanism of ethene oligomerization catalyzed by Ni-SSZ-24 zeolite, as well as the formation of the active site. After comparing three possible catalytic cycles, they concluded the most probable reaction path to be the Cossee-Arlman mechanism and that the support is involved in the active site formation [15].

The metallacycle mechanism has recently been proposed for ethene oligomerization by Andrei et al. over Ni-AlSBA-15. The authors suggested two types of mechanisms: the metallacycle mechanism for oligomerization of ethene and a second mechanism based on acid catalysis for isomerization of products. The Cossee-Arlman mechanism was concluded as unlikely because of the absence of co-catalysts in these reactions [16].

The aim of the current study was to compare the performance of Ni-based catalysts based on zeolite supports and dense, mesoporous supports, respectively, under similar reaction conditions. A further aim of the study was to characterize the active sites of zeolite-based catalysts by FTIR spectroscopy

and elucidate mechanistic details of the ethene oligomerization reaction through contact time variation experiments.

1. Experimental

1.1. Catalyst preparation

Microcrystalline NH_4-Beta zeolite (Si/Al) = 19) was obtained from Zeolyst (CP-814C). The NH_4-Beta sample was calcined at 550 °C for 6 h using a heating rate of 1.5 °C/min to obtain the protonated form. The resulting material is denoted H-Beta(m).

Nanocrystalline Na-Beta zeolite (Si/Al = 13) was obtained from PQ. The Na-Beta sample was calcined at 550 °C for 3 h using a heating rate of 1 °C/min (denoted Na-Beta(n)) before ion exchange. The catalyst was subjected to three consecutive ion exchanges with 1M NH_4NO_3 at 70 °C for 2 h using a liquid to solid ratio of 20 cm^3/g, then dried overnight. The exchange was then followed by calcination at 550 °C for 8 h, using a heating rate of 5 °C/min to obtain the protonated form. The resulting material is denoted H-Beta(n).

The nickel ion exchanged zeolite samples were prepared as described by Martinez et al. [13]. The zeolite sample was subjected to four consecutive ion exchanges with intermediate drying steps at 100 °C. The exchanges were carried out with 0.1 M aqueous solution of $Ni(NO_3)_2$ at 70 °C for 4 h using a liquid-to-solid-ratio of 10 cm^3/g. Subsequently, the material was calcined at 550°C for 3h using a heating rate of 1°C/min. The material obtained by ion exchange and calcination of H-Beta(m) is denoted Ni-H-Beta(m). The material obtained by ion exchange and calcination of Na-Beta(n) is denoted Ni-H(Na)-Beta(n)(2), while the material obtained by ion exchange and calcination of H-Beta(n) is denoted Ni-H-Beta(n) and Ni-H-Beta(n)(2) with 2 and 4 wt % Ni, respectively.

2 wt. % $NiSO_4$-SiO_2-Al_2O_3 and 2 wt. % $NiSO_4$-Al_2O_3 catalysts were prepared as previously described in detail by Lu et al. [17]. SiO_2-Al_2O_3 and γ-Al_2O_3 supports were impregnated with an aqueous solution of nickel sulfate ($NiSO_4$) followed by drying over night at 105 °C and calcination in air at 400 °C for 2 hours.

1.2. Catalyst characterization

The phase identification of the zeolite samples was performed by X-ray powder diffraction (PXRD) measurements. A Bruker D8 Discover diffractometer was employed, using Cu K_α radiation (λ = 1.5406 Å).

The textural properties of the samples were derived from N_2 adsorption isotherms, measured at -196 °C, using a BELSORP-mini II instrument. All samples were outgassed in vacuum for 1 h at 80 °C and 3 h at 300 °C, and then measured. The catalyst pore volumes and surface areas were determined using the t-plot and BET methods.

Scanning electron microscopy (SEM) was performed by using a Hitachi SU8230 microscope; the characterization parameters are included in the images.

Elemental analysis was performed on Agilent 4100 MP-AES instrument after dissolving the catalyst in 1 mL 15 wt % HF.

The nature of the active sites was investigated by FTIR spectroscopy. The experiments were carried out in transmission mode using a Nicolet 6700 FTIR spectrometer (Thermo Scientific) equipped with a mercury cadmium telluride (MCT) cryodetector working with 2 cm^{-1} resolution. Thin self-supporting wafers of each sample (H-Beta(m) and Ni-H-Beta(m)) were placed inside a flow IR cell designed to allow high temperature treatment under gas flow and *ex-situ* low-temperature IR measurements. Prior to adsorption experiments, samples were thermally treated in He flow (50 mL/min) up to 300 °C and left at this temperature for 3 hours, in order to mimic the activation conditions used in the catalytic tests. In order to investigate the role of Ni sites in the oligomerization reaction, in one experiment Ni-H-Beta(m) sample was subsequently cooled down to 150 °C, and then contacted with a flow of ethene (20 mL/min) and helium (50 mL/min) for 30 min. After activation, the cell was moved to the IR instrument (in controlled atmosphere) to carry out measurements at low temperature (liquid nitrogen temperature, LNT). Activated samples were kept in He (or He/C_2H_4) atmosphere (slight overpressure) until connection to the vacuum line. Before CO dosage the catalysts were then outgassed at room temperature (RT) to remove He or He/C_2H_4 atmosphere.

CO adsorption experiments were carried out at LNT by sending 30 Torr of CO on the zeolites activated as described above, followed by stepwise decrease of the pressure. For all samples, the spectrum before CO dosage was used as reference to obtain the subtracted spectra reported in the CO stretching region (νCO). For comparison spectra were normalized by employing the fingerprint region of silicate frameworks in the 1750–2100 cm^{-1} region (overtone and combination modes of framework vibrations).

The concentration of acid sites was investigated with FT-IR spectroscopy using pyridine as probe molecule. The measurements were performed in transmission mode on a Bruker Vertex 80 instrument with a Mercury Cadmium Telluride (MCT) detector. For this purpose, a quartz cell with KBr windows was employed. Catalysts were prepared as thin wafers supported in a gold envelope and pre-treated in vacuum (<10^{-5} mbar) for 3 hours: 1 hour at 150 °C followed by 2 hours at 300 °C. The adsorption of pyridine was done by exposing the pellets to pyridine vapor. After equilibration at room temperature, the catalysts were degassed at 200 °C for 2 h. The final spectrum was recorded at RT and the integrated area of the bands at 1545 and 1455 cm^{-1} with molar extinction coefficients of 0.73 and 0.64 were used to determine the amounts of Brønsted and Lewis acid sites, respectively.

1.3. Catalytic testing

Catalytic tests were carried out in a continuous flow, fixed bed, stainless steel reactor. Before each experiment, the catalyst was pressed, crushed and sieved to 240-420 µm grain size. The catalyst mass (100-200 ± 5 mg) was adjusted to obtain partial conversion (below 20 %). The catalyst was loaded in the reactor and was activated in-situ at 300 °C for 16 h under 1 bar of helium. The total pressure was then increased in He (up to 30 bar) and controlled by a back-pressure regulator (Bronkhorst P-702CV). During reaction, the partial pressures were controlled by adjusting individual flows. The desired mixture of ethene (provided by AGA, 2.5 grade), inert and internal standard (10 % Ne in He, provided by AGA, 2.5 grade) was fed through the reactor, keeping the total pressure constant, but varying the partial pressure of ethene. Typical reaction conditions were: 120 °C with a total pressure of 29 bar and with a contact time of 0.0068 $min.g_{cat}.mL^{-1}$ or 0.0034 $min.g_{cat}.mL^{-1}$ (at STP). The experiments used the following reference condition: T = 120 °C, P(total) = 29 bar where P_{ethene} = 25.1 bar and P_{inert} = 3.9 bar. Each experiment started under reference conditions and then returned to reference conditions between each change of conditions. The reference conditions were then used to simulate a deactivation model and to correct for the deactivation (see Figure SI 1 for an example). In this contribution, such correction was only employed in the partial pressure variation experiments (Section 2.3.3), since the conversion level under reference conditions was rather constant in the contact time variation experiments (Section 2.3.4).

A small portion of the reactor effluent, about 4 mL/min, was led through heated lines to an online gas chromatograph (Agilent 7890B) equipped with three columns: CP-Molsieve 5A (50 m x 0.53 mm x 50 µm) connected to TCD, GS-Gaspro (60 m x 0.32 mm) and DB-1 (40 m x 0.10 mm x 0.20 µm) both

connected to FID. The three channels were used for detection of neon, light hydrocarbons up to butenes and heavier hydrocarbons, respectively. This made it possible to analyze all effluent products simultaneously (without the need to condense the heavy products), while the presence of Ne as an internal standard allowed for calibration to obtain accurate mass balances.

Ethene conversion and product selectivity were calculated by using the following formulas:

$$Conversion\ (\%) = \ (1 - \frac{[Ethene_{out}]}{[Ethene_{in}]} * \frac{Vout}{Vin}) \cdot 100 \quad (1)$$

Where [$Ethene_{in}$] is determined by feed analysis and V_{out}/V_{in} is determined by [Ne_{in}]/[Ne_{out}].

$$Selectivity\ (i)(\%) = \frac{[Product(i)]}{\sum_n [Product(n)]} \quad (2)$$

2. Results and discussion

2.1. Catalyst characterization

The main physical properties of the catalysts are summarized in Table 1. X-ray Diffractograms (XRD) of the zeolite samples are shown in Figure 1. Scanning Electron Microscopy (SEM) images of two representative samples (Ni-H-Beta(m) and Ni-H-Beta(n)(2)) are shown in Figure 2.

Looking first at Figure 1, the XRD patterns confirmed that all zeolite samples belong to the BEA framework. No changes in the intensity or the position of the diffraction peaks were observed after calcination and/or ion exchange, assessing the absence of degradation during preparation. Martinez et al. [13] reported diffraction peaks at 37.2° and 43.3° for Ni-impregnated, nanocrystalline Beta samples and ascribed them to crystalline nickel oxide (NiO). However, no such peaks were observed in the samples prepared in the present study. Considering next the results presented in Figure 2, the SEM images confirmed the micro- and nanocrystalline size of Ni-H-Beta(m) and Ni-H-Beta(n)(2), respectively. The particle size distribution of Ni-H-Beta(n)(2) was narrow and below 50 nm, while the particle size for Ni-H-Beta(m) ranged from 100 to 700 nm. The nickel distribution in each sample was investigated by mapping different regions of the samples. For Ni-H-Beta(m), Ni-containing particles with less than 20 nm diameter were observed on the zeolite surface, ascribed to NiO. These nanoparticles were not observed with XRD most probably due to the low amount present in the

sample. No NiO particles were detected for Ni-H-Beta(n)(2) (see Figure SI 2 for backscattered electron images).

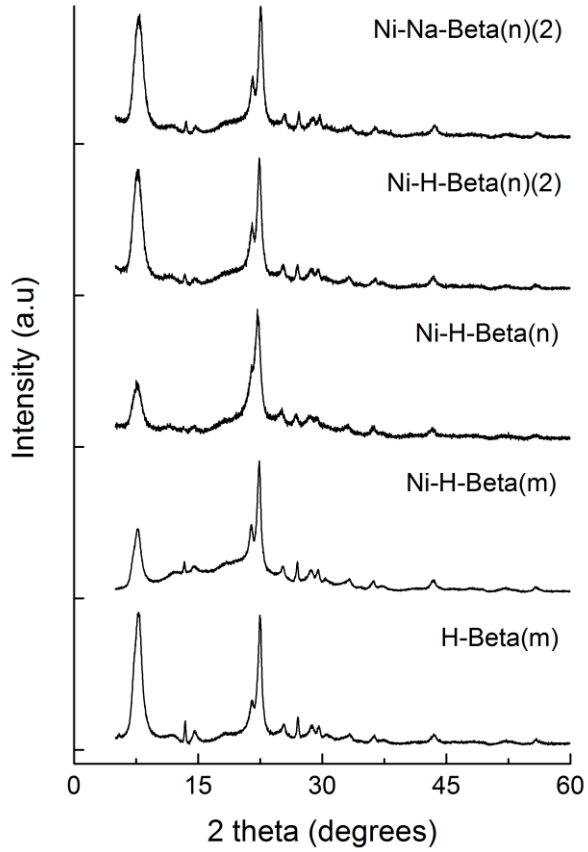

Figure 1: X-ray diffraction patterns for zeolite catalysts

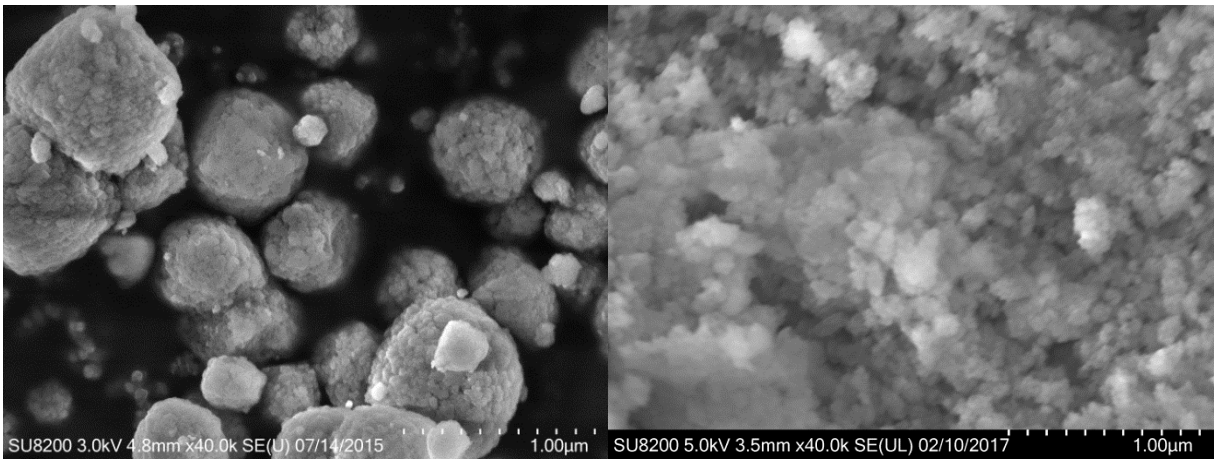

Figure 2: Scanning Electron Microscopy images of Ni-H-Beta(m) (left) and Ni-H-Beta(n)(2) right. Identical scaling was used to highlight the difference in crystal size between the samples

In Table 1, it is observed that all zeolite samples had high and similar specific surface areas (S_{BET}), as expected for such highly crystalline structure. All nanocrystalline samples (n) exhibited one order of magnitude higher mesoporous volume (V_{meso}) compared to the microcrystalline samples (m). Comblor et al. [18] have shown that decreasing the crystal size increases the mesoporous volume observed in adsorption isotherms, and assigned this effect to inter-particular space and to agglomeration. On the right side of the table, the elemental analysis shows that, for all measured zeolite samples, the silicon to aluminum ratio increased slightly after ion exchange, suggesting that aluminum was lost during the treatment. This is most likely extra-framework aluminum that was washed away during ion exchange, as further supported by FT-IR (see below).

The amount of Brønsted and Lewis acid sites (BAS and LAS, respectively) for the zeolite catalysts was determined by FT-IR-pyridine and is shown in Table 1. The parent samples contained both BAS and LAS; the LAS were possibly due to extra-framework Al species. Upon ion exchange with Ni^{2+}, the amount of BAS decreased, compared to the parent micro- and nanocrystalline H-Beta catalysts, indicating that Ni^{2+} is exchanged with the Brønsted acid sites. Furthermore, the LAS were shifted towards lower frequencies and increased in abundance upon Ni^{2+} exchange. This shift is illustrated in Figure 3, where in addition to the band at 1622 cm^{-1} ascribed to pyridine coordinated to aluminum species, a new band at 1610 cm^{-1} is observed. This band is only present in the Ni-exchanged catalysts and is attributed to pyridine coordinated to Ni^{2+} cations [19, 20]. However, the Ni/Al ratio of some of the catalysts was above 1, suggesting that Ni is also present in another form, such as NiO observed on the surface of Ni-H-Beta(m) with SEM (Figure SI 2) or Ni^{2+} sites grafted to defective silanol groups [43]. Even though no NiO was observed for nanocrystalline catalysts, we cannot discard its presence completely. As a final note, a sample denoted Ni-H(Na)-Beta(n)(2) was prepared by ion exchange of the calcined Na-Beta(n) sample. The aim was to compare a sample containing Ni sites but not proton sites, to the Ni- and proton-containing samples. Surprisingly, the pyridine adsorption experiments revealed that the amount BAS of Ni-H(Na)-Beta(n)(2) was higher than in Ni-H-Beta(n)(2). This result indicates that during Ni-exchange, sodium is not only exchanged with nickel, but also with protons. Similar results have been reported for Y zeolite, where the introduction of divalent cations (Ca^{2+}, Mg^{2+}, Ni^{2+}) also introduced BAS [21]. Thus, with these catalysts, isolating and studying nickel in BAS free catalyst would require a different procedure.

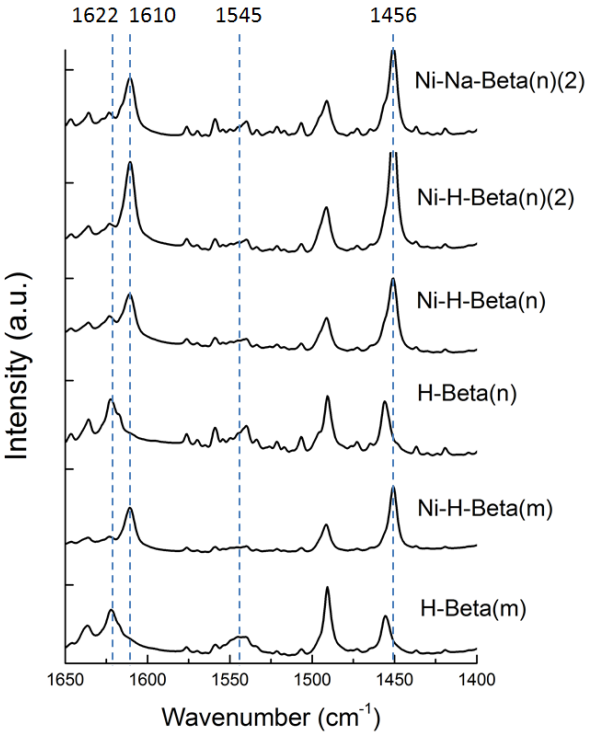

Figure 3: Spectra of the pyridine region after pyridine desorption at 200 °C

Table 1: Textural properties and elemental composition for all catalysts

	S_{BET} (m^2/g)	V_{micro} (cm^3/g)	V_{meso} (cm^3/g)	Si/Al	Ni/Al	Ni (wt. %)	BAS mmol/g	LAS mmol/g
H-Beta(m)	677	0.28	0.08	19.7	-	-	0.55	0.49
Ni-H-Beta(m)	651	0.28	0.17	24.0	1.2	2.2	0.19	0.92
Na-Beta(n)	712	0.27	0.76	13.5	-	-		
H-Beta(n)	677	0.19	0.80		-	-	0.65	0.68
Ni-H-Beta(n)	570	0.18	0.58	17.4	0.83	2.1	0.29	1.20
Ni-H(Na)-Beta(n)(2)	616	0.23	0.73	17.5	1.76	4.2	0.42	1.37
Ni-H-Beta(n)(2)	620	0.22	0.69	15.8	1.73	4.6	0.26	1.41
$NiSO_4$-Al_2O_3	193	0.01	0.66	-	-	2.0		
$NiSO_4$-SiO_2-Al_2O_3	454	0.03	0.55	-	-	2.0		

2.2. FTIR: pursuing the active site(s)

FTIR spectroscopy was employed to gain insight about the active site(s) on the catalyst. We initially characterized the different Ni sites present in the pristine catalysts. The catalysts were characterized again after reaction with ethene, leading us to propose both active and spectator sites.

2.2.1. νOH region: ion exchange of nickel sites

The vOH vibrational region of activated H-Beta(m) and Ni-H-Beta(m) samples are shown in Figure 4. In both spectra, absorption bands at 3740, 3662 and 3610 cm^{-1} are observed, while H-Beta(m) also shows a weak band at 3782 cm^{-1}. The band at 3745 cm^{-1} is related to isolated silanol groups on the external zeolite surface. The two components at 3782 at 3662 cm^{-1} are typical of OH groups related to extraframework Al atoms [22], even if features in the 3720 - 3620 cm^{-1} range have also been observed in defective Al-free silicalites, and assigned to internal silanols in different environments [23]. Noticeably, after Ni exchange the band at 3782 cm^{-1} specifically assigned to OH groups on tricoordinated Al atom partially linked to the framework [22], disappears. This is in agreement with the increase of Si/Al ratio observed by elemental analysis (Table 1). The typical vOH band of Si(OH)Al Brønsted sites is found at 3610 cm^{-1}. After Ni exchange, the relative intensity of the band related to Brønsted acid sites decreased, as expected. However, ion exchange is not complete, and a significant fraction of Brønsted sites is still present, as confirmed by pyridine adsorption experiments.

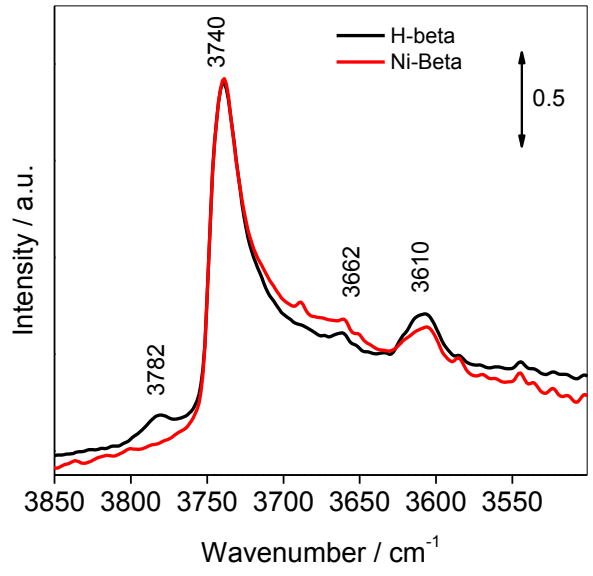

Figure 4: IR spectra in the vOH region of dehydrated H-Beta(m) and Ni-H-Beta(m) samples

2.2.2. Adsorbed species after ethene contact

As described in experimental section, Ni-H-Beta(m) sample was contacted with ethene at 150 °C for 30 min. The IR spectra after and before ethene contact are shown in Figure 5. Bands related to CH_3 and CH_2 groups could be observed in both stretching (2956, 2927, 2873 and 2856 cm^{-1}) and bending (1406, 1380 and 1366 cm^{-1}) regions. Other weak bands are observed at 1503 and 1534 cm^{-1}. Bands in similar positions have been assigned to unsaturated carbocations [24].Coke analysis of the spent catalysts (Figure SI 4) showed no aromatics detected by GC-MS, even after dissolution of the materials in HF. These results suggest that the adsorbed compounds are mainly aliphatic hydrocarbons.

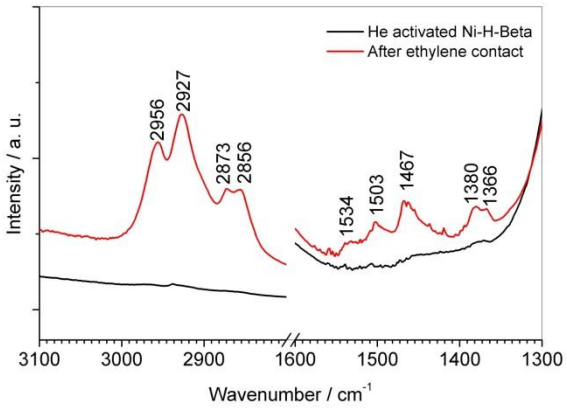

Figure 5: Adsorbed species formed on Ni-H-Beta(m) sample after contact with ethene/He mixture at 150 °C for 30 min

2.2.3. Ni species: active and spectator sites

Infrared spectroscopy of CO adsorbed at low temperature (LNT, around -196 °C) was utilized to investigate the different types of Ni surface sites available before and after ethene contact (Figure 6). Data obtained on H-Beta(m) sample are also reported for comparison. Low temperature experiments were carried out according to Martinez et al. [13], who reported that upon room temperature CO contact Ni^{2+} sites could be reduced to Ni^{+}, thus affecting the interpretation. However our recent investigations on Ni-containing ZSM-5 [25] showed that if Ni content is low (less than 2%), reduction of Ni^{2+} by CO at room temperature does not occur.

High coverage CO spectra (not shown) were characterized for all samples by the typical bands related to CO adducts with Brønsted sites (2176 cm^{-1}), silanols (2157 cm^{-1}) and by the typical band of physisorbed CO ('liquid-like', 2141 cm^{-1}) [25, 26]. These are the only ones present on Ni-free sample (H-Beta, top panel of Figure 6). For the sake of brevity, only the spectra measured at relatively low CO coverage (θ_{CO}) are reported and discussed, since they provide most information about the nature of Ni sites. These are reported in Figure 6 for Ni-H-Beta(m) sample activated in He/ethene or He flows (top and middle, respectively) and for on H-Beta(m) activated in He (bottom), for comparison. In all panels of Figure 6 the spectra measured at the highest considered θ_{CO} (0.1 mBar) are reported in red; blue spectra are related to intermediate coverage, allowing to better appreciate spectra evolution with pressure (0.01-0.005 mBar); finally, black curves were measured while outgassing the sample under dynamic vacuum (residual pressure $1*10^{-4}$ mBar).

Concentrating on He activated Ni-H-Beta(m) sample (middle panel), new features are observed at high frequency at 2212 (weak), 2202 and 2195 cm^{-1} (shoulder), which gradually decrease with θ_{CO}. These are in the typical region of CO adducts on Ni^{2+} sites and were assigned to complexes formed on two distinct Ni^{2+} counterions (2212 and 2202 cm^{-1}) and on grafted Ni^{2+} sites (2195 cm^{-1}) [25, 27-29]. Moving to lower frequency, the band at 2150 cm^{-1}, disappearing upon θ_{CO} decrease, was observed upon CO adsorption on low surface area NiO particles, suggesting the presence of small (not detected by XRD, see above) nickel oxide particles [30]. Bands at lower frequency are in the spectral region typical of CO adducts on Ni^{+} and Ni^{0} particles [13, 25, 31, 32]. More in detail, at intermediate coverage (blue spectrum) very weak features are observed at 2138 and 2095 cm^{-1}. Under dynamic vacuum (black curve) broad bands are formed with maxima at 2148, 2116 and 2092 cm^{-1}, with a broad tail extending to lower wavenumbers. The nature of these bands will be discussed in more detail. For the moment, it is enough to mention that they indicate that some reduction of Ni^{2+} upon activation in inert He atmosphere has occurred, as observed elsewhere [25].

The top panel of Figure 6 shows the CO spectra measured in similar conditions on Ni-H-Beta(m) sample after ethene contact. First, we note the decrease in intensity of the bands at 2176 and 2162 cm^{-1}, related to CO adducts on Brønsted and silanols, indicating an interaction of ethene with these sites. Concerning the bands assigned to Ni ions, we note that the bands related to Ni^{2+} counterions (2202 and 2215 cm^{-1}) are no longer present, as opposed to those related to grafted Ni^{2+} sites and NiO small particles. Additionally, an increase in the intensity of the bands related to reduced Ni sites (2157, 2138, 2120, 2112 and 2092 cm^{-1}) is observed. While the bands at 2157, 2120 and 2112 cm^{-1} decrease in intensity, the couple at 2138 and 2092 cm^{-1} first increases (maximum intensity at 0.01 mbar, blue curves) and then decreases. This transformation could be explained by a $Ni^{+}(CO)_3$ to $Ni^{+}(CO)_2$ transformation, as reported by Penkova *et al*. on reduced Ni-Beta [32]. The same authors reported the

occurrence of an equilibrium between $Ni^{+}(CO)_2$ and $Ni^{+}(CO)$ adducts when the experiment was carried out at RT, with the latter giving a band at 2113 cm^{-1}. The reported results clearly show a reductive effect of ethene, with formation of highly coordinatively unsaturated Ni^{+}, which are thus likely to be present as counterions. Noticeably, even if a small amount of $Ni^{+}(CO)_2$ complexes could be inferred also on the sample activated in He (middle panel, blue curve, bands at 2138 and 2092 cm^{-1}), in that case we could not exclude the formation of Ni^{0} particles, as suggested by the broad tail below 2100 cm^{-1}, increasing when reducing CO pressure, as often observed in the presence of metal pariticles [31]. This suggest that the reduction mechanism in the presence of inert atmosphere and ethene is different.

It remains elusive how ethene reduces exchanged Ni^{2+} to Ni^{+}; it is insufficient to explain it by an electron transfer from ethene to Ni, as it does not take into account how the excess zeolite framework charge is compensated for. Based on our recent theoretical work [24], we suggest an alternative explanation: what appears to be a reduction of exchanged Ni^{2+} to Ni^{+} ions on the basis of IR data, could instead be related to active sites formed by reaction of ethene with the Ni^{2+} ions (Scheme 2) [24]:

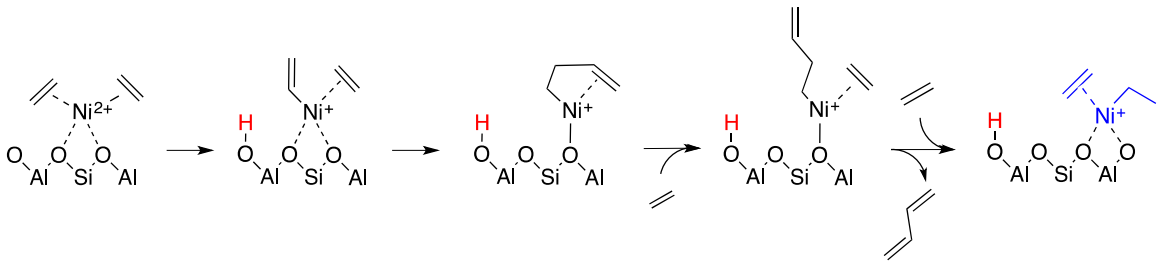

Scheme 2: Formation of the active site

When the cell is evacuated after contact with ethene, excess ethene and alkyl groups are removed, reducing these Ni^{2+} sites to isolated Ni^{+} ions analogously to how $[Cu(II)\text{-}OH]^{+}$ is reduced to Cu^{+} in vaccuum [33].

Summarizing, the results may be explained by a mechanism where ethene reacts with Ni^{2+} counter ions to form Cossee-Arlman oligomerization sites, while Ni sites grafted and on the surface of small NiO particles are spectator species. We acknowledge the recent results by Moussa et al., who proposed a higher activity for Ni sites on the surface of NiO particles, on sample with relatively high Ni content (5%) [16]. However, in conjunction with previous work [13] our results indicate that NiO species can be considered 'spectators' in the ethene oligomerization reaction.

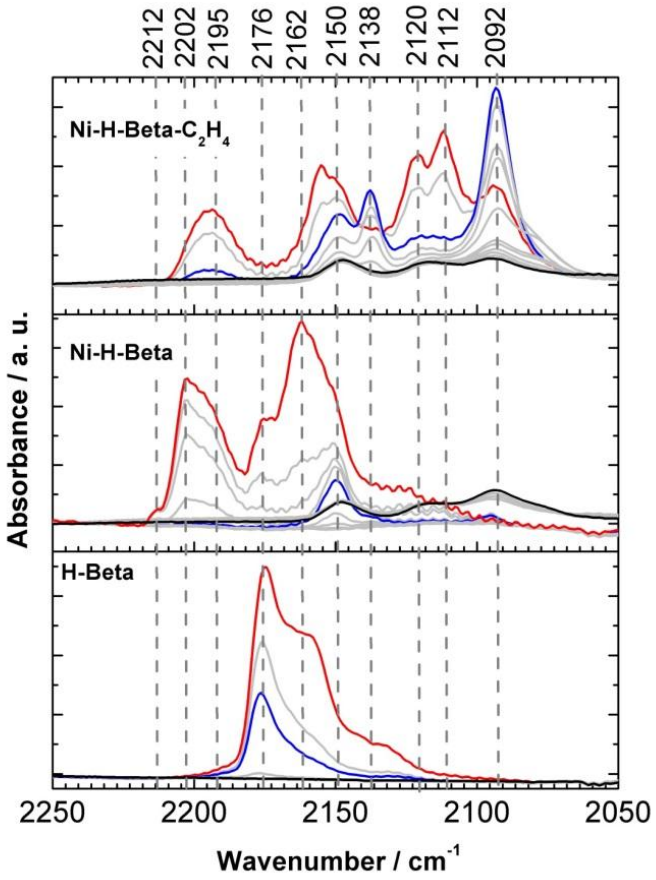

Figure 6: Low coverage CO spectra measured at LNT on: top) Ni-H-Beta(m) sample activated in He/ethene flow at 150 °C; middle) Ni-H-Beta(m) sample activated in He flow at 300 °C and bottom) H-Beta(m) sample activated in He flow at 300 °C. Red curves correspond to the highest CO pressure (0.1 mBar), blue curves to intermediate coverage allowing to appreciate spectra evolution (0.01-0.005 mBar), black spectra were measured under dynamic vacuum (residual pressure 1 10^{-4} mBar).

2.3. Catalytic testing

2.3.1. Influence of active site. Ni-H-Beta(m) versus H-Beta(m)

The nickel ion exchanged samples contain two different types of active sites; nickel (oxidation state 0, +I or +II) and Brønsted acid sites. These sites have been reported to show different activity and selectivity for the ethene oligomerization reaction under identical reaction conditions [11]. To elucidate the respective roles of nickel and proton sites under the conditions used in the present study, experiments were carried out with Ni-H-Beta(m) and H-Beta(m). Ethene conversion and linear butene

selectivity obtained over the two samples at 120, 200 and 300 °C are shown in Figure 7. Over H-Beta(m), the initial ethene conversion was 5 % at 120 °C, i.e. the standard reaction temperature in the present study, and 4 % at 200 °C. Over Ni-H-Beta(m), the initial ethene conversion was 22 % at 120 °C and 34 % at 200 °C. These results show that the initial activity of the proton sites for ethene oligomerization is low compared to the nickel sites under the conditions studied here.

Considering product selectivity, it should be noted that not all products formed are gaseous: some carbon-containing products were not detected by GC-FID, but were quantified from mass balance (denoted retained hydrocarbons, R-HC). Small amounts of gaseous hexene (below 5 % selectivity) were also detected; for clarity, this amount was lumped with the R-HC fraction. For example, with H-Beta(m), the selectivity towards gaseous products was below 1 % at 120°C, and around 20 % at 200 °C (see Figure SI 3 for selectivity versus time on stream).

In terms of linear butenes selectivity over the two samples, the initial selectivity was 27 % over Ni-H-Beta(m), and less than 1 % over H-Beta(m) at 120 °C. At 200 °C, this increased to 76 % and 2 %, respectively. While the by-products of Ni-H-Beta(m) were exclusively longer, linear, even carbon-numbered alkenes, the effluent of H-Beta(m) included a variety of linear, branched alkanes and alkenes, mostly between C_3 and C_6. The selectivity towards these products is consistent with the presence of acid sites in the zeolite, catalyzing oligomerization reactions as well as proton transfer, isomerization and cracking reactions [34].

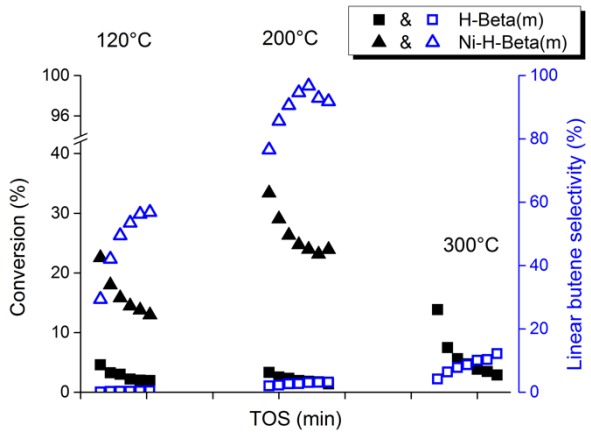

Figure 7: Ethene conversion (solid symbols) and linear butene selectivity (hollow symbols) at 120 – 200 – 300 °C versus time on stream. Reaction conditions: m_{cat} = 0.200 g, contact time: 0.0067 g·min/mL at STP, 29 bar total pressure where P_{ethene} = 21.2 bar and P_{inert} = 7.8 bar for H-Beta(m) and P_{ethene} = 25.1 bar and P_{inert} = 3.9 bar for Ni-H-Beta(m)

To highlight the differences in selectivity over the two materials, the integrated yields of linear and branched C_4 products during 1260 min on stream are shown in Table 2. Over H-Beta(m), the production of linear and branched alkenes are of the same order of magnitude, at both temperatures. This observation is in agreement with literature data: Brønsted acid sites are expected to promote the carbenium ion mechanism, favoring the production of branched aliphatic products [35]. In addition to butenes, the selectivity towards iso-butane was significant, at approximately 20 %, suggesting the presence of hydrogen transfer on the Brønsted acid sites [36].

Over Ni-H-Beta(m), the integrated yield of branched alkenes and alkanes is negligible compared to the production of linear butenes. The results obtained show that the Ni sites dominate as ethene oligomerization sites on Ni-H-Beta(m) under the conditions used in the present study.

Table 2: Integrated yield (mg) of linear and branched butenes produced during 1260 min time on stream. Reaction conditions: m_{cat} = 0.200 g, contact time = 0.0067 g·min/mL at STP, 29 bar total pressure where P_{ethene} = 21.2 bar and P_{inert} = 7.8 bar for H-Beta(m) and P_{ethene} = 25.1 bar and P_{inert} = 3.9 bar for Ni-H-Beta(m)

	$T_{reaction}$ = 120 °C		$T_{reaction}$ = 200 °C	
	Linear-$C_4^=$ (mg)	Branched $C_4^=$ (mg)	Linear-$C_4^=$ (mg)	Branched $C_4^=$ (mg)
H-Beta(m)	0.4	0.3	21	43
Ni-H-Beta(m)	490	0.4	1250	3.4

2.3.2. Influence of support topology and morphology. Ni-H-Beta(m), Ni-H-Beta(n), Ni-H(Na)-Beta(n) and $NiSO_4$-(SiO_2)-Al_2O_3

Initial ethene conversion rates obtained over the Ni-containing catalysts under standard conditions (120 °C, P_{ethene} = 25.1 bar) are plotted versus time on stream in Figure 8.

The zeolite catalysts showed rapid initial deactivation, followed by a period of slower deactivation. Such behavior is typical of processes where product deposition is responsible for catalyst deactivation [37]. The lower conversion rate of Ni-H-Beta(m) compared to Ni-H-Beta(n) is mainly ascribed to the particle size as the amount of nickel, BAS and LAS is similar in the two materials (Table 1). Larger crystallites (Ni-H-Beta(m)) present a longer diffusion path. Transport of the reactant and products between the active sites and the surface is limited [38], leading to build-up of larger products inside the pores and finally deactivation. Comparing Ni-H-Beta(n) with 2 wt % Ni to Ni-H-Beta(n)(2) and Ni-H(Na)-Beta(n)(2) with 4 wt % Ni shows that the conversion rate is almost unaffected by the nickel

amount. This result suggests that different nickel species are present in the catalyst and that only nickel in certain environment/configuration is active for ethene oligomerization as previously reported by Martinez et al. [13].

After a short period of deactivation, around 120 min, the activity of the mesoporous catalyst ($NiSO_4/Al_2O_3$ and $NiSO_4/SiO_2$-Al_2O_3) increased for several hours before subsequently decreasing again. Such behavior is typical of systems where active sites are initially formed or gradually become accessible for the reactants at a higher rate than the rate of deactivation, until deactivation dominates, in this case after approximately 200 and 500 min on stream for $NiSO_4/Al_2O_3$ and $NiSO_4/SiO_2$-Al_2O_3, respectively. This pattern has already been observed in propene oligomerization by Mlinar et al. [39]. In that work, the authors argue that the activation period is due to the migration of nickel ions in the lattice of faujasite; this interpretation cannot be directly applied to the $NiSO_4$-containing catalysts used in this study as they do not present the same microporous structure. Another possible explanation is that the initiation period is due to the slow build-up of active sites, which may involve formation of Ni-C bond and breakage of Ni-O bond [15, 40, 41].

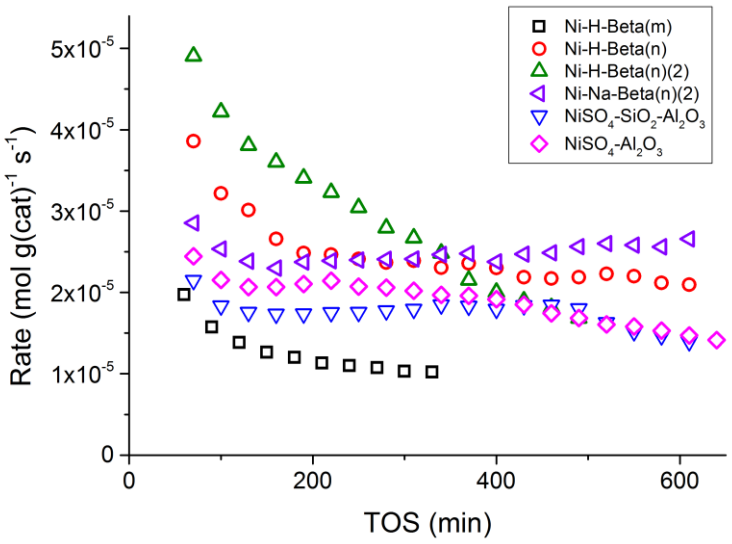

Figure 8: Rate versus time on stream for all catalysts. Reference reaction conditions: 29 bar total pressure where P_{ethene} = 25.1 bar and P_{inert} = 3.9 bar and T = 120 °C

The linear butene selectivity observed during the initiation period is reported in Figure 9. The data were obtained during the same tests shown in Figure 8, i.e. with deactivating catalysts. All catalysts showed high linear butene selectivity, while only traces of alkanes and odd carbon number products were formed, indicating that acid-catalyzed side reactions are not occurring to a significant extent. Furthermore, no trace of iso-butene was observed. The hydrocarbons R-HC retained in Ni-H-Beta(n)

were characterized, and were found to consist of long chained even-numbered alkenes (see Figure SI 4 for GC-MS analysis of the spent catalysts). The absence of odd numbered products in R-HC further supports that the acid sites are not active to a significant degree.

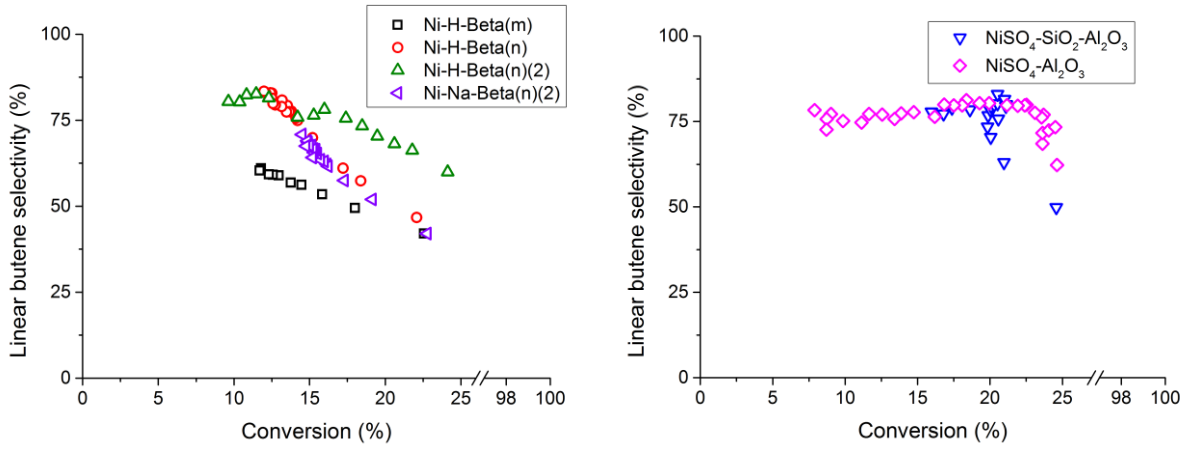

Figure 9: Linear-$C_4^=$ selectivity versus conversion for zeolite (left) and $NiSO_4$-containing (right) catalysts. Reference reaction conditions: 29 bar total pressure where P_{ethene} = 25.1 bar and P_{inert} = 3.9 bar and T = 120 °C

Concentrating first on the four zeolite-based catalysts (Figure 9**,** left panel), butene selectivity steadily increased with a decrease in conversion. This result may suggest that not only ethene, but also product butene and possibly higher alkenes, may adsorb and be converted on the active sites of the catalyst. However, it could also mean that the active sites are changing with deactivation. At any given conversion, butene selectivity was lower for microcrystalline Ni-H-Beta(m) than for nanocrystalline Ni-H-Beta(n), hence the selectivity towards heavier products, including R-HC, is higher. This difference may be explained again by the difference of particle size. Because of the longer diffusion path in larger particles (Ni-H-Beta(m)), the transport of the primary product, butene, from the active sites to the external bulk phase is hindered [42]; this longer residence time in the pores likely favors secondary reactions and formation of longer chains. The longest of these secondary products are permanently stuck in the pores, as the relatively fast deactivation rate and the GC-MS analyses of the spent catalysts suggest. Secondly, larger particles (Ni-H-Beta(m)) have significantly lower external surface, and the selectivity of the external nickel sites is expected to yield formation of smaller products than inside the pores, because of the absence of stabilization of longer aliphatics.

Concentrating next on the mesoporous catalysts (Figure 9**,** right panel), a different pattern was observed: an increase in butene selectivity was observed during the activation period for each catalyst. This observation suggests that not only the amount, but also the nature of the active sites change during the activation period [43]. During the subsequent period of deactivation, no change in butene

selectivity was observed upon decreasing conversion. This result is in accordance with data published by Toch et al. for a Ni/SiO_2-Al_2O_3 catalyst [14]. They observed that product selectivity is independent of ethene conversion, leading to Anderson-Schulz-Flory product distribution [44].

Likewise, the difference observed between the microporous (left panel) and mesoporous (right panel) catalysts may be due to a different reaction mechanism, or to the enhanced diffusion restrictions in the microporous catalyst, which is likely to increase the abundance of secondary reactions.

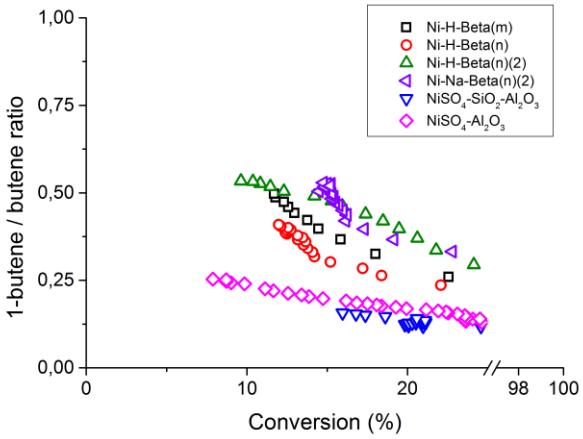

Figure 10: 1-butene/(1- and 2-butene) ratio versus conversion for all catalysts. Reference reaction conditions: 29 bar total pressure where P_{ethene} = 25.1 bar and P_{inert} = 3.9 bar and T = 120 °C

To further elaborate on selectivity differences between the materials, 1-butene/total butene ratio versus ethene conversion is shown in Figure 10. The plots are divided into two groups: first, the 1-butene/total butene ratio over zeolite catalysts increased steadily with decreasing conversion, suggesting initially high rate for isomerization of 1-butene or high initial formation of 2-butenes. The other group comprises the two mesoporous catalysts, $NiSO_4/Al_2O_3$ and $NiSO_4/SiO_2$-Al_2O_3. Over these catalysts, the 1-butene/total butene ratio was lower than for zeolite catalyst and increased only slightly with decreasing conversion. Under these conditions, the equilibrium 1-butene/total linear butene ratio is approximately 0.07 [45]. The mesoporous catalysts are closer to thermodynamic equilibrium and this suggests a much higher isomerization rate compared to the ethene oligomerization rate over these catalysts. The evolution of butene selectivities with conversion for the zeolite catalysts will be discussed further in section 2.3.4

2.3.3. Partial pressure variation experiments

To further elucidate the effect of catalyst topology, the five catalysts were subjected to ethene partial pressure variation tests at 120 °C in order to derive the reaction order of ethene in the rate of consumption of ethene. Distinct differences were observed between the microporous and mesoporous catalysts. The ethene oligomerization reaction was second order over the microporous catalysts, while it was closer to one (1.2 and 1.4) over the mesoporous catalysts. The latter agrees reasonably well with previous work of Toch et al, who observed a first order dependency on P_{ethene} on Ni/SiO_2-Al_2O_3, for P_{ethene} between 1.5 – 3.5 bar [14].

Next, we focus on the reaction order of ethene in the rate of production of butenes, in order to obtain mechanistic insight in the dimerization reaction. The results are reported in Figure 11 and summarized in Table 3. It is instructive to consider the mechanistic implication of the reaction order depending on the catalyst topology. Considering first the Cossee-Arlman mechanism of Scheme 1, theoretical work from Brogaard and Olsbye found that [Ni-alkene-alkyl] species have quite similar stability in the SSZ-24 microporous zeolite [24]. This means that in the Cossee-Arlman mechanism, the resting state of the catalyst can easily change from [Ni-ethene-ethyl], giving a reaction order of 0, to a [Ni-alkene-alkyl] species resulting in a reaction order of 2 in ethene for the rate of butene production. It is reasonable to expect a higher reaction order in the microporous zeolites, where alkyl chains are significantly stabilized, than on mesoporous catalysts where such stabilization is significantly less. This is consistent with the higher reaction orders obtained experimentally with the Beta zeolites, around 2, than on the $NiSO_4$-containing materials, between 1.5 and 1.7 (the uncertainties being high, as the conversion at P_{ethene} = 9 bar is below 5 %). However, a similar change in reaction order could also be consistent with the metallacycle mechanism, for the same reason: longer alkenes adsorb on the Ni sites in the micropores, leading to a second order dependence in ethene for butene production, which could decrease towards first (zeroth) order on a catalyst without stabilization from pores, having a Ni-ethene (dimer) species as resting state.

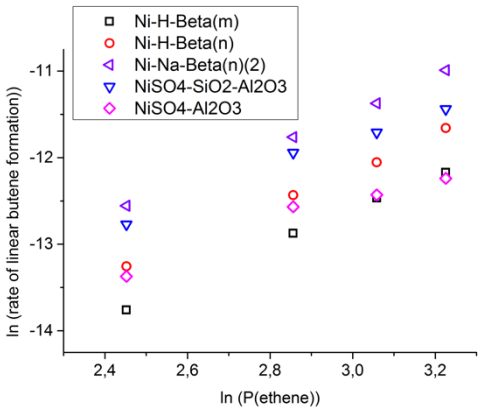

Figure 11: Logarithm plot of butenes production rate for all catalysts, as a function of logarithm of partial pressure of ethene at T = 120°C

Table 3: Reaction order with respect to ethene for the rate of production of butenes, for the investigated catalysts. Reaction conditions: T = 120 °C, 29 bar total pressure where P_{ethene} = 25.1-11.6 bar and P_{inert} = 3.9-17.4 bar

Catalyst	Ethene consumption	Butene formation
Ni-H-Beta(m)	2	2.0
Ni-H-Beta(n)	2	2.0
Ni-H(Na)-Beta(n)(2)	2	2.0
$NiSO_4$–Al_2O_3	1.2	1.5
$NiSO_4$–SiO_2–Al_2O_3	1.4	1.7

2.3.4. Steady state performance

It was discussed in section 2.3.2 that the selectivities among butenes vary with conversion during the initiation phase. The evolution of yields as a function of ethene conversion, obtained by contact time variation under steady state conditions, can give us a better insight into the primary and secondary products, as well as into the potential presence of different active sites. A new series of experiments was therefore carried out with the Ni-H-Beta(m), Ni-H-Beta(n), Ni-H-Beta(n)(2) and Ni-H(Na)-Beta(n)(2) catalysts at lower ethene partial pressure (P_{ethene} = 17.4 bar and P_{inert} = 11.6 bar, T = 120 °C). 1-butene and 2-butenes selectivities during the initial deactivation period (insets) and in steady state (main plots) is shown in Figure 12. Overall, the trends are very similar among the four catalysts.

The initial performance for all catalysts changed in a similar manner as observed in the tests at P_{ethene} = 26 bar: 1-butene yield increases with deactivation, which may suggest that the nature of the active

sites changes through time, or that some secondary reaction sites producing 2-butenes from 1-butene, such as Brønsted acid sites, deactivate.

On the other hand, the steady state plots suggest that all butene yields follow a straight line going through the origin. This indicates that all three linear butenes are primary products; hence only one type of active site is involved in the conversion of ethene to butenes, at least after the first deactivation period. This observation is in best agreement with the Cossee-Arlman mechanism: which accounts for the formation of 2-butenes, while the metallacycle mechanism cannot account for the formation of 2-butenes (Scheme 1).

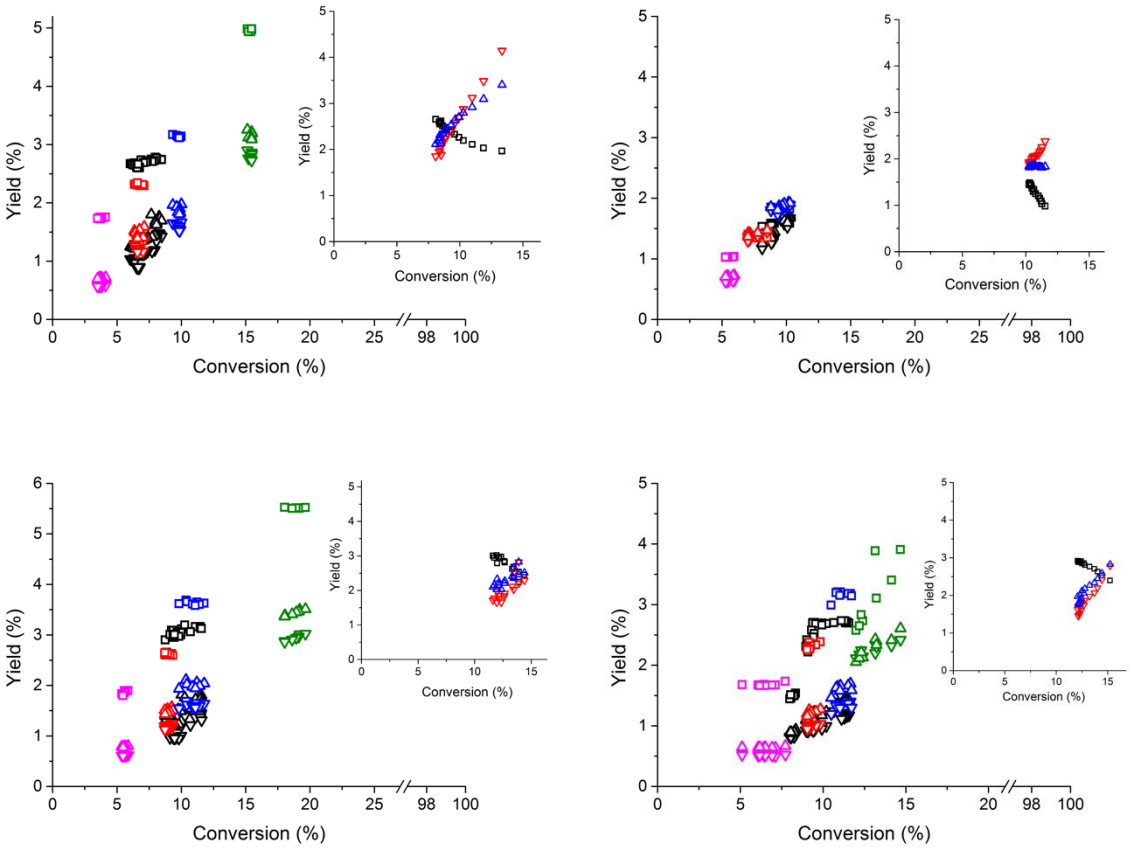

Figure 12: Yield (%) (square: 1-butene, up triangle: cis-2-butene, down triangle: trans-2-butene) as a function of conversion for a) Ni-H-Beta(m), b) Ni-H-Beta(n), c) Ni-H-Beta(n)(2), d) Ni-H(Na)-Beta(n)(2). Reaction conditions: 29 bar total pressure where P_{ethene} = 17.4 bar and P_{inert} = 11.6 bar, T = 120 °C. Contact time varied between 0.002 – 0.008 for nanocrystalline and between 0.004 – 0.016 g_{cat}*min/mL for microcrystalline catalysts, the results from each contact time measurement are represented by a different colour.

Conclusion

Nickel-containing mesoporous ($NiSO_4$-SiO_2-Al_2O_3/$NiSO_4$-Al_2O_3) and microporous (microcrystalline Ni-H-Beta and nanocrystalline Ni-H/Na-Beta) catalysts were prepared by ion exchange of commercial catalysts. Characterization of the materials by N_2 sorption showed predictably that the Beta zeolites have a much higher microporous volume than the amorphous supports. Moreover, SEM and elemental analysis revealed that the amount of nickel present was 2-4 wt. % depending on the sample. One sample (Ni-H-Beta(m)) showed notably presence of nickel oxide clusters.

Ethene oligomerization tests were performed at 29 bar and 120 °C in a plug flow fixed bed reactor. Significant differences were identified between the catalysts in sense of activity, selectivity and reaction order. These results depended especially on porosity and particle size. First, the results obtained with the different zeolite samples emphasized the role of nickel as the active site for oligomerization of ethene as the amount of ethene converted at Brønsted acid sites was found to be negligible. Another finding is that crystal size has a large impact on deactivation, because of diffusion limitations associated with the formation of long chain products eventually leading to the build-up of products inside the pores. Secondly, the mesoporous catalysts presented a period of activation, attributed to the formation of the active sites by contact of $NiSO_4$ with the reactant. Also, the product selectivities were quite different from the zeolites; stable $C_4^=$ selectivity with deactivation was rapidly achieved. Furthermore, the 1-butene to total butene ratio was closer to thermodynamic equilibrium over these catalysts than over the microporous catalysts.

The initial change in product selectivity during deactivation of the zeolite catalysts indicates that they initially had more than one active site, but only one active site was remaining after the initial deactivation period. Based on contact time variation experiments, all three linear butenes were found to be primary products, in accordance with the Cossee-Arlman mechanism.

FTIR spectroscopy confirmed the presence of a variety of Ni species in sample Ni-H-Beta(m), including two distinct Ni^{2+} counterions, grafted Ni^{2+}, small NiO particles and possibly a very small amount of Ni^0 particles. Measurements carried out to probe the sites accessible to the CO probe after interaction with ethene showed that only ion exchanged nickel, under +II oxidation state, and Brønsted acid sites allow adsorption and reaction of ethene in the described conditions, ruling out the participation of NiO or grafted nickel in the process.

Acknowledgments

This research was funded by the Research Council of Norway through the OLIGOM project (224980).

References

1. *IEA's Key World Energy Statistics.* 2015.
2. Jacob A. Moulijn, M.M., Annelies E. van Diepen, *Chemical Process Technology, 2nd Edition*. 2013: John Wiley and Sons.
3. Breuil, P.-A.R., L. Magna, and H. Olivier-Bourbigou, *Role of Homogeneous Catalysis in Oligomerization of Olefins : Focus on Selected Examples Based on Group 4 to Group 10 Transition Metal Complexes.* Catalysis Letters, 2014. **145**(1): p. 173-192.
4. Finiels, A., F. Fajula, and V. Hulea, *Nickel-based solid catalysts for ethylene oligomerization - a review.* Catalysis Science & Technology, 2014. **4**(8): p. 2412-2426.
5. McGuinness, D.S., *Olefin Oligomerization via Metallacycles: Dimerization, Trimerization, Tetramerization, and Beyond.* Chemical Reviews, 2010. **111**(3): p. 2321-2341.
6. Sohn, J.R., W.C. Park, and S.-E. Park, *Characterization of Nickel Sulfate Supported on SiO2–Al2O3 for Ethylene Dimerization and Its Relationship to Acidic Properties.* Catalysis Letters, 2002. **81**(3): p. 259-264.
7. Heveling, J., C.P. Nicolaides, and M.S. Scurrell, *Catalysts and conditions for the highly efficient, selective and stable heterogeneous oligomerisation of ethylene.* Applied Catalysis A: General, 1998. **173**(1): p. 1-9.
8. Hulea, V. and F. Fajula, *Ni-exchanged AlMCM-41—An efficient bifunctional catalyst for ethylene oligomerization.* Journal of Catalysis, 2004. **225**(1): p. 213-222.
9. Lallemand, M., et al., *Continuous stirred tank reactor for ethylene oligomerization catalyzed by NiMCM-41.* Chemical Engineering Journal, 2011. **172**(2–3): p. 1078-1082.
10. Andrei, R.D., et al., *Heterogeneous oligomerization of ethylene over highly active and stable Ni-AlSBA-15 mesoporous catalysts.* Journal of Catalysis, 2015. **323**: p. 76-84.
11. Heveling, J., A. van der Beek, and M. de Pender, *Oligomerization of ethene over nickel-exchanged zeolite y into a diesel-range product.* Applied Catalysis, 1988. **42**(2): p. 325-336.
12. Lallemand, M., et al., *NiMCM-36 and NiMCM-22 catalysts for the ethylene oligomerization: Effect of zeolite texture and nickel cations/acid sites ratio.* Applied Catalysis A: General, 2008. **338**(1–2): p. 37-43.
13. Martínez, A., et al., *New bifunctional Ni–H-Beta catalysts for the heterogeneous oligomerization of ethylene.* Applied Catalysis A: General, 2013. **467**: p. 509-518.
14. Toch, K., J.W. Thybaut, and G.B. Marin, *Ethene oligomerization on Ni-SiO2-Al2O3: Experimental investigation and Single-Event MicroKinetic modeling.* Applied Catalysis A: General, 2015. **489**: p. 292-304.
15. Brogaard, R.Y. and U. Olsbye, *Ethene Oligomerization in Ni-Containing Zeolites: Theoretical Discrimination of Reaction Mechanisms.* ACS Catalysis, 2016: p. 1205-1214.
16. Moussa, S., et al., *Heterogeneous oligomerization of ethylene to liquids on bifunctional Ni-based catalysts: The influence of support properties on nickel speciation and catalytic performance.* Catalysis Today.
17. Li, L., R.D. Palcheva, and K.-J. Jens, *Conversion of Ethene to Propene by a Dual Function NiSO4/Re2O7/γ-Al2O3 Catalyst.* Topics in Catalysis, 2013. **56**(9): p. 783-788.
18. Camblor, M.A., A. Corma, and S. Valencia, *Characterization of nanocrystalline zeolite Beta.* Microporous and Mesoporous Materials, 1998. **25**(1–3): p. 59-74.

19. Brückner, A., et al., *The role of different Ni sites in supported nickel catalysts for butene dimerization under industry-like conditions.* Journal of Catalysis, 2009. **266**(1): p. 120-128.
20. Vázquez, M.I., A. Corma, and V. Fornés, *Characterization of NiO supported on zeolite Y, by pyridine adsorption.* Zeolites, 1986. **6**(4): p. 271-274.
21. Ward, J.W., *The nature of active sites on zeolites.* Journal of Catalysis, 1968. **10**(1): p. 34-46.
22. Marques, J.P., et al., *Infrared spectroscopic study of the acid properties of dealuminated BEA zeolites.* Microporous and Mesoporous Materials, 2003. **60**(1–3): p. 251-262.
23. Bordiga, S., et al., *Characterisation of defective silicalites.* Journal of the Chemical Society, Dalton Transactions, 2000(21): p. 3921-3929.
24. Palumbo, L., et al., *Conversion of Methanol to Hydrocarbons: Spectroscopic Characterization of Carbonaceous Species Formed over H-ZSM-5.* The Journal of Physical Chemistry C, 2008. **112**(26): p. 9710-9716.
25. Ganjkhanlou, Y., et al., *Incorporation of Ni into HZSM-5 zeolites: Effects of zeolite morphology and incorporation procedure.* Microporous and Mesoporous Materials, 2016. **229**: p. 76-82.
26. Bleken, B.-T.L., et al., *Probing the surface of nanosheet H-ZSM-5 with FTIR spectroscopy.* Phys. Chem. Chem. Phys., 2013. **15**: p. 13363-13370.
27. Mihaylov, M. and K. Hadjiivanov, *FTIR Study of CO and NO Adsorption and Coadsorption on Ni-ZSM-5 and Ni/SiO_2.* Langmuir, 2002. **18**: p. 4376-4383.
28. Hadjiivanov, K., et al., *Characterization of Ni/SiO_2 Catalysts Prepared by Successive Deposition and Reduction of Ni^{2+} Ions.* J. Catal., 1999. **185**: p. 314-326.
29. Hadjiivanov, K., H. Knozinger, and M. Mihaylov, *FTIR Study of CO Adsorption on Ni-ZSM-5.* J. Phys. Chem. B, 2002. **106**: p. 2618-2624.
30. Zecchina, A., et al., *Surface structures of oxides and halides and their relationships to catalytic properties.* Adv. Catal., 2001. **46**: p. 265-397.
31. Gopalakrishnan, S., et al., *Unravelling the structure and reactivity of supported Ni particles in Ni-CeZrO2 catalysts.* Applied Catalysis B: Environmental, 2013. **138–139**: p. 353-361.
32. Penkova, A., et al., *Effect of the Preparation Method on the State of Nickel Ions in BEA Zeolites. A Study by Fourier Transform Infrared Spectroscopy of Adsorbed CO and NO, Temperature-Programmed Reduction, and X-Ray Diffraction.* The Journal of Physical Chemistry C, 2007. **111**(24): p. 8623-8631.
33. Borfecchia, E., et al., *Revisiting the nature of Cu sites in the activated Cu-SSZ-13 catalyst for SCR reaction.* Chemical Science, 2015. **6**(1): p. 548-563.
34. Xu, B., et al., *Catalytic activity of Brønsted acid sites in zeolites: Intrinsic activity, rate-limiting step, and influence of the local structure of the acid sites.* Journal of Catalysis, 2006. **244**(2): p. 163-168.
35. sanati, M., C. Hornell, and S.G. Jaras, *The oligomerization of alkenes by heterogeneous catalysts*, in *Catalysis: Volume 14*. 1999, The Royal Society of Chemistry. p. 236-288.
36. Nivarthy, G.S., et al., *The role of hydride transfer in zeolite catalyzed isobutane/butene alkylation*, in *Studies in Surface Science and Catalysis*, F.V.M.S.M. Avelino Corma and G.F. José Luis, Editors. 2000, Elsevier. p. 2561-2566.
37. Bartholomew, C.H., *Mechanisms of catalyst deactivation.* Applied Catalysis A: General, 2001. **212**(1–2): p. 17-60.

38. Wulfers, M.J. and R.F. Lobo, *Assessment of mass transfer limitations in oligomerization of butene at high pressure on H-beta.* Applied Catalysis A: General, 2015. **505**: p. 394-401.
39. Mlinar, A.N., et al., *Propene oligomerization over Ni-exchanged Na-X zeolites.* Journal of Catalysis, 2012. **296**(0): p. 156-164.
40. Mlinar, A.N., et al., *Selective Propene Oligomerization with Nickel(II)-Based Metal–Organic Frameworks.* ACS Catalysis, 2014: p. 717-721.
41. !!! INVALID CITATION !!! {}.
42. Reddy, J.K., et al., *Effect of morphology and particle size of ZSM-5 on catalytic performance for ethylene conversion and heptane cracking.* Journal of Catalysis, 2012. **289**(0): p. 53-61.
43. Lu Li, S.C., Elena Groppo, Einar Sagstuen, Silvia Bordiga, Unni Olsbye, Klaus-Joachim Jens, *Characterization of the NiSO4 site on a NiSO4-ReOx/γ-Al2O3 catalyst for tandem conversion of ethylene to propylene.* Catalysis Science & Technology, 2016. **Manuscript submitted for publication**.
44. Britovsek, G.J.P., et al., *Ethylene Oligomerization beyond Schulz–Flory Distributions.* ACS Catalysis, 2015. **5**(11): p. 6922-6925.
45. Alberty, R.A. and C.A. Gehrig, *Standard Chemical Thermodynamic Properties of Alkene Isomer Groups.* Journal of Physical and Chemical Reference Data, 1985. **14**(3): p. 803-820.

Supporting information

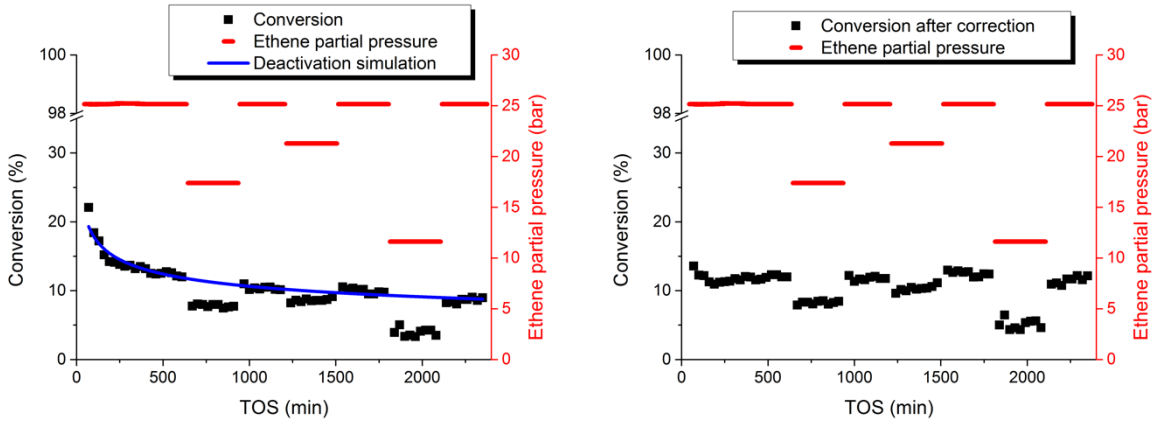

Figure SI 1: Left: Deactivation simulation based on standard condition (29 bar total pressure where P_{ethene} = 25.1 bar and P_{inert} = 3.9 bar and T = 120 °C). Right: Conversion versus TOS, after correcting for deactivation

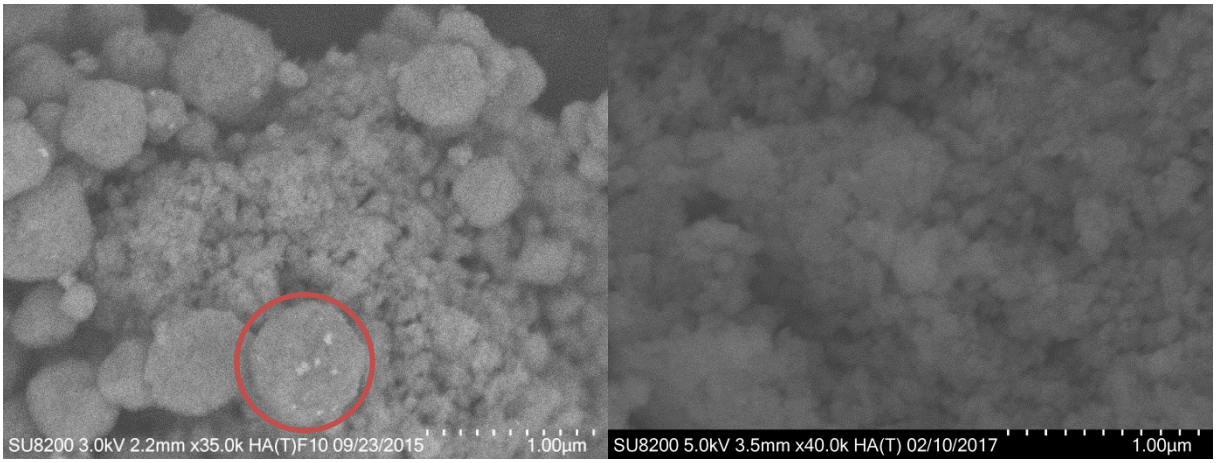

Figure SI 2: Backscattered electron picture of Ni-H-Beta(m) (left) and Ni-H-Beta(n)(2) (right)

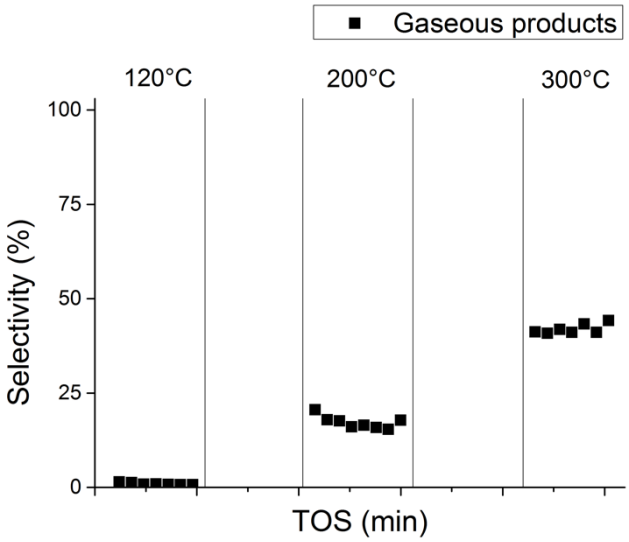

Figure SI 3: Selectivity towards gaseous products at 120, 200 and 300°C for H-Beta(m)

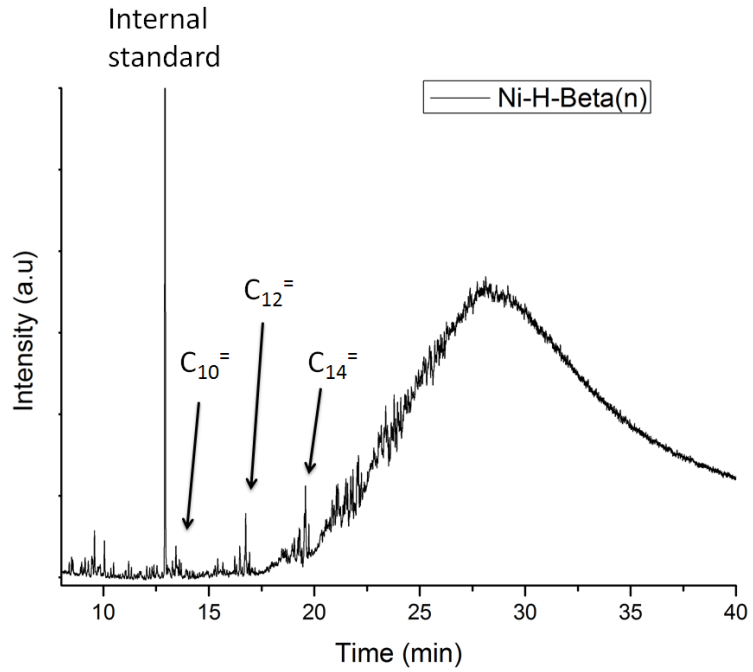

Figure SI 4: Gas chromatogram of the retained hydrocarbons in the spent Ni-H-Beta(n) catalyst, extracted in dichloromethane